




Evaluation of spray pyrolysed In:ZnO nanostructures for CO gas sensing at low concentration

Aninamol Ani¹, P. Poornesh^{1,*} , K. K. Nagaraja^{1,3}, Gopalkrishna Hegde², E. Kolesnikov³, Igor V. Shchetinin³, Albin Antony¹, and Suresh D. Kulkarni⁴

¹Department of Physics, Manipal Institute of Technology, Manipal Academy of Higher Education, Manipal, Karnataka 576104, India

²Department of Nano-Sciences, Indian Institute of Science, Bengaluru, Karnataka 560 012, India

³National University of Science and Technology 'MISIS', Leninskiy Pr. 4, Moscow 119049, Russian Federation

⁴Department of Atomic and Molecular Physics, Manipal Academy of Higher Education, Manipal, Karnataka 576104, India

Received: 19 April 2021

Accepted: 31 July 2021

Published online:

10 August 2021

© The Author(s) 2021

ABSTRACT

Herein, we report the role of indium (In) on the carbon monoxide sensing of ZnO thin films using a low-cost spray pyrolysis technique. The decrease in crystalline size was observed from XRD studies and hexagonal wurtzite structure was confirmed. Photoluminescence and XPS studies proved the presence of various defects in the films. The gas-sensing properties of films toward carbon monoxide (CO) gas indicate that 15 wt% of In in ZnO thin films (IZO) exhibit high response (1.84) to a low concentration of the gas (1 ppm) at 300 °C compared to undoped ZnO (0.53). The observed high response of 15 wt% IZO can be mainly endorsed to the oxygen vacancy defects as observed from the photoluminescence and XPS analysis. Further, the high response is complemented by high surface area and smaller grain size (~ 13.1 nm) with well-defined grain boundaries as evident from SEM analysis as well as XRD studies.

1 Introduction

Air pollution has been increased in a large amount in recent years due to rapid industrialization and urbanization. Highly flammable, toxic, and hazardous gases such as carbon monoxide (CO), carbon dioxide (CO₂), hydrogen sulfide (H₂S), sulfur dioxide (SO₂), ammonia (NH₃), liquefied petroleum gas (LPG), etc. are causing environmental contamination at an alarming rate [1–5]. Among the mentioned

gases, carbon monoxide can be detrimental to human beings as it plays a significant role in contributing to polluting the atmospheric air due to the high amount of combustion processes [6]. As a result of combustion from motor vehicles and industries, CO is released into the atmosphere at an alarming rate. It is a poisonous gas with no color, odor, and taste, and therefore, it is difficult to detect, particularly in low concentrations [7]. Above 15 ppm, it is reported that inhalation of CO affects the human body at a dangerous level [8]. A single exposure to CO in large

Address correspondence to E-mail: poorneshp@gmail.com; poornesh.p@manipal.edu

doses is acute and repeated exposure to CO in low levels for a long time is chronic. CO combines with hemoglobin and forms carboxyhemoglobin thereby decreasing the oxygen transport capacity of the blood [9, 10]. Studies indicate that the threshold limit value (ACGIH) of CO gas is 25 ppm [11]. Also, several deaths have been reported recently due to the leakage of CO gas from electric appliances such as heater. Therefore, the active and timely detection of CO gas at a low concentration level is a pressing need at present. Henceforth, different types of gas sensors are developed to sense the harmful CO gas.

Among the different kinds of gas sensors, metal oxide semiconductor (MOS)-based gas sensors have gained extensive attention because of its high selectivity, sensitivity, ability to sense a wide variety of gases, and low fabrication cost [12–15]. They possess high surface area, high electron mobility, and excellent catalytic properties [16]. MOS-based resistive gas sensors also called as chemiresistive sensors are extensively used due to its simple operation along with enhanced sensing properties. They are devices that produce a measurable electrical signal upon exposure to a chemical environment containing gases [17]. Tungsten oxide (WO_3), tin oxide (SnO_2), titanium oxide (TiO_2), and zinc oxide (ZnO) are some of the most recognized gas-sensing metal oxide semiconductors [18, 19]. However, ZnO stands out as a capable candidate for gas sensor applications owing to its exceptional material properties. It is an II–VI wide bandgap semiconductor. It occurs naturally as n-type and stable chemically as well as thermally. ZnO possesses high mobility, optically transparent in the visible region, and is one of the finest sensors for an extensive range of both reducing and oxidizing gases and the ease of preparation and availability in abundance makes it a suitable contender [20–24].

Hjiri et al. fabricated aluminum (Al)-doped ZnO sensor [25] and indium (In)-doped ZnO sensor [26] by sol–gel route technique for detection of CO in the range of (5–50) ppm at various operating temperatures from 250 to 300 °C. They optimized the temperature to be 300 °C and found the response to a low concentration of 5 ppm for both the dopants. They had also studied the response of pristine ZnO nanoparticles toward CO concentrations of (5–50) ppm at 350 °C [27]. Dhahri et al. [28] deposited In-doped ZnO nanoparticles and found the response at 350 °C toward CO concentrations of (5–50) ppm. Pan and Zhao [29] performed on-chip sensing toward

250 ppm and 500 ppm of CO gas at room temperature by ZnO nanocomb-based gas sensors. However, all these studies report the sensing of CO gas concentrations above 5 ppm. Paliwal et al. [30] fabricated ZnO -based optical sensors for CO detection and recorded the sensing to (0.5–100) ppm gas concentrations from the change in reflectance. However, fabrication of optical gas sensors involves relatively high cost and complex instrumentation compared to MOS-based gas sensors.

In this study, low concentrations of CO-sensing properties of indium-doped ZnO (IZO) thin films prepared via spray pyrolysis method are presented. Spray deposition was adopted to develop the sensing layer due to its flexibility in scaling to industrial manufacturing [31, 32]. To date, there are no reports on CO gas sensing at lower concentrations below 5 ppm by resistive-based ZnO gas sensor. The detection at the lowest level is significant because of the hazardous nature of the CO gas. Indium is chosen as the dopant since it has proven itself as an effective element to enhance the electronic properties of ZnO [33]. Close examination of the literatures proves that indium is an excellent dopant in enhancing the oxygen vacancies in the sensing layer which plays a critical role in improved sensitivity toward CO gas. Tan et al. [34] reported the improvement in oxygen vacancies upon In doping in ZnO nanorods, thereby facilitating the excellent CO-sensing performance. Moreover, gas-sensing analysis of spray-coated IZO thin films is not well reported except a few studies on the sensing of CO gas above 5 ppm. In this work, we successfully synthesized In-doped ZnO -sensing layer that could detect a low concentration of 1 ppm of CO gas.

2 Experimental specifics

2.1 Preparation of IZO thin films

The precursors used for the synthesis of undoped and IZO thin films were zinc acetate dihydrate [$(\text{CH}_3\text{COO})_2\text{Zn}\cdot 2\text{H}_2\text{O}$] and indium(III) nitrate hydrate ($\text{InN}_3\text{O}_9\cdot x\text{H}_2\text{O}$). At room temperature, zinc acetate dihydrate of 0.05 M concentration was dissolved in double-distilled water and a homogenous solution is obtained after stirring magnetically. The indium doping was achieved at fixed doping concentrations of 5 wt%, 10 wt%, and 15 wt% by adding

a solution of indium nitrate hydrate dissolved in double-distilled water to the host solution. The final solution was sprayed onto a soda-lime glass substrate which was ultrasonically cleaned by spray pyrolysis. The substrate temperature was held at 425 °C. The film thickness was kept to be around ~ 300 nm measured using a thickness profilometer. Further increase in indium doping resulted in a non-uniform formation of the film as well as a slow adsorption process. The illustration of precursor solution preparation and synthesis of IZO thin films by spray pyrolysis deposition is shown in Fig. 1.

2.2 Material characterization

The dopant-induced structural variations in ZnO films were analyzed by glancing angle X-ray diffraction (GAXRD). The linear optical measurements were obtained using UV–visible spectrometer given in S1 of Supporting Information and surface morphological variations were studied from atomic force microscope (AFM) using Bruker Icon in tapping mode and scanning electron microscopy (SEM). The several defects responsible for the gas sensing are investigated by employing photoluminescence (PL) spectroscopy technique. X-ray photoelectron spectroscopy (XPS) were performed to determine the chemical states of Zn, O and In in the deposited films.

2.3 Gas sensing measurements

Conducting silver paste was used to make Ohmic contacts to serve as the electrodes. The undoped and IZO sensors were placed in sequence in a gas chamber (3.05×10^{-4} cm³ in volume). Mass flow controllers were utilized to monitor the mixing ratio of CO gas and dry air (20% oxygen and 80% nitrogen) in required concentrations. The whole flow of gases was kept at 500 sccm. Dry air was purged in a controlled manner to the chamber to stabilize the sensor resistance. The operating temperature was optimized by analyzing sensor responses at different temperatures. The CO gas was purged to the chamber in required concentrations by diluting with synthetic air and the change in the resistance of the sensor in the air and CO was noted continuously at the optimized temperature for sensing measurements. The resistance change was measured using a Keithley 2450 source meter. The CO gas concentrations were maintained from 1 to 5 ppm at an interval of 1 ppm. The recovery time and the response time of the IZO sensor on exposure to different CO gas concentrations were computed. The schematic arrangement of measurement set-up for sensing is shown in Fig. 2.

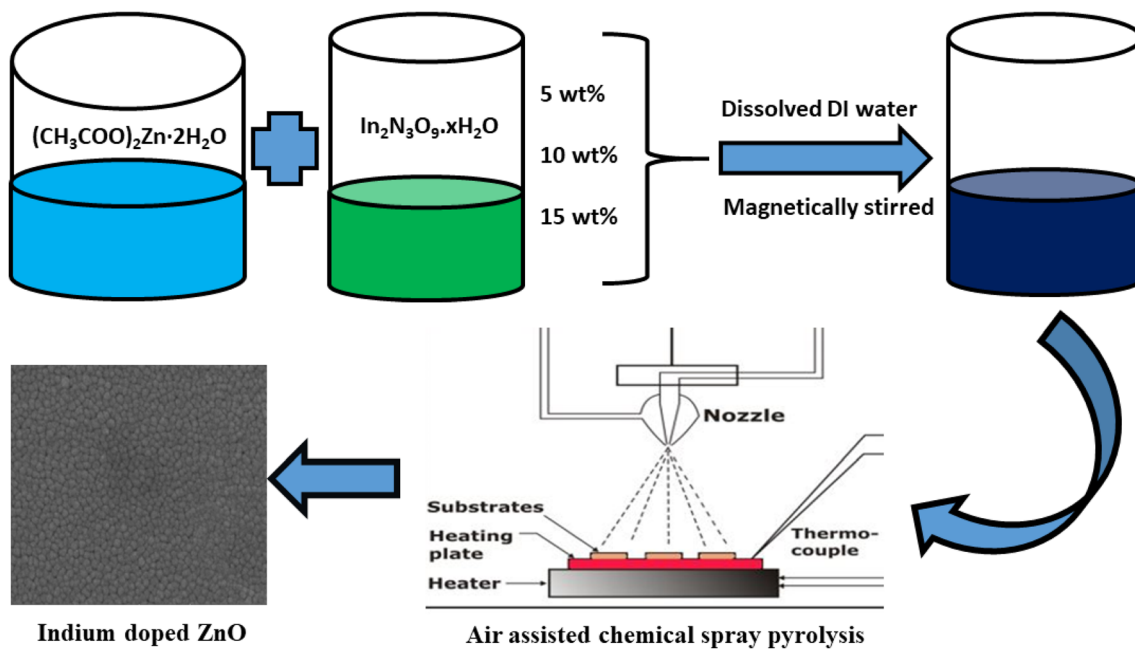


Fig. 1 Illustration of precursor solution preparation and synthesis of IZO thin films

3 Results and discussions

3.1 Structural investigations

The obtained films are polycrystalline and the diffraction peaks correspond to hexagonal wurtzite structure with space group $P63mc$ (JCPDS card file 36-1451). The obtained peaks correspond to (002), (100), (101), (102), (103) (110) (112) planes of ZnO. All the GAXRD patterns were observed to be preferentially oriented toward the most intense (101) plane. The observed peak intensity varies with the concentration of doping owing to the reduction in crystalline size which causes a decrease in the peak intensity in the preferred orientation. Also, it is evident that upon 15 wt% In doping the intensity of (100) and (002) peaks has increased. A rise in the indium doping concentration causes a peak broadening in the most intense diffraction peak which could be related to the generation of strain in the films since In^{3+} has a larger ion radius (0.080 nm) than Zn^{2+} (0.074 nm) [35–37].

XRD patterns of undoped and IZO films are depicted in Fig. 3. Various microstructural parameters obtained from X-ray characterization are presented in Table 1. Scherrer equation was employed to determine the crystalline size [38] given by,

$$D = \frac{k\lambda}{\beta \cos\theta}. \quad (1)$$

The strain was calculated from the formula [39] and observed to be increased upon In doping.

$$\varepsilon = \frac{\beta \cos\theta}{4}. \quad (2)$$

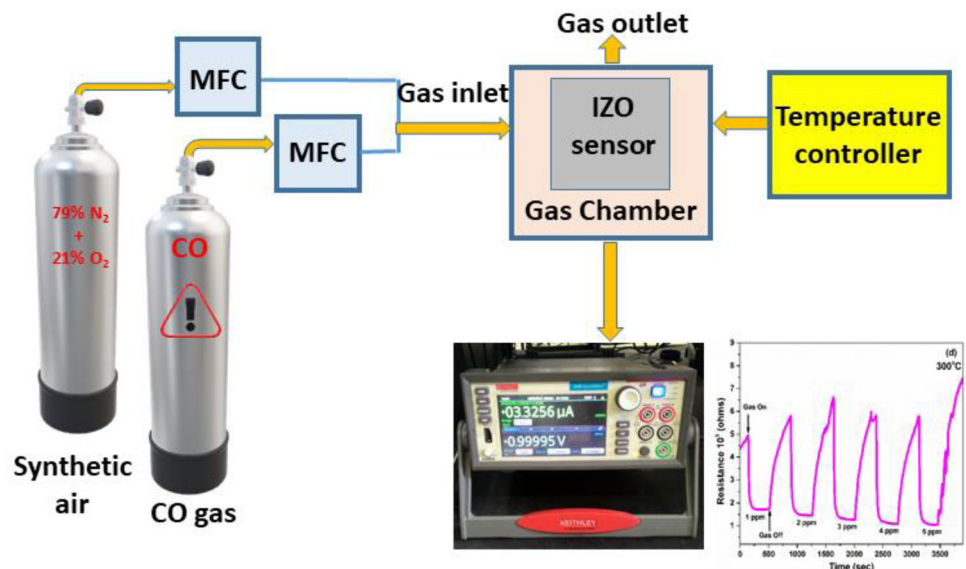
The comparison of the XRD data of Indium oxide (In_2O_3) with 15 wt% IZO is included in S2 of Supporting Information.

3.2 Morphological investigations

The surface morphological studies of the films were analyzed by AFM and SEM techniques and shown in Fig. 4. A top view of the images clearly shows that the results are in decent agreement with each other for undoped and doped films.

The RMS values of the roughness of the films were computed by Nanoscope Analysis using AFM micrographs. The values are in the range 8 to 28 nm indicating the smooth nature of the films. The RMS roughness values are 28.4 nm for undoped, 10.6 nm for 5 wt%, and 10 wt% and 8.18 nm for 15 wt% IZO films. The grains in undoped film exhibit pea-shaped structure and upon increasing indium concentration, the films are gaining hexagonal shape as evident from SEM analysis. The grain size is reducing upon indium doping with an increase in grain boundaries and it is in line with the XRD results obtained. The 15 wt% IZO film has a large surface area and many grains with well-defined grain boundaries compared to other films. This aids in providing more sites that are active for gas adsorption which in turn boosts the response toward the target gas [40]. The impact of nanograins on the gas-sensing properties of ZnO

Fig. 2 Schematic arrangement of the gas sensor measurement system



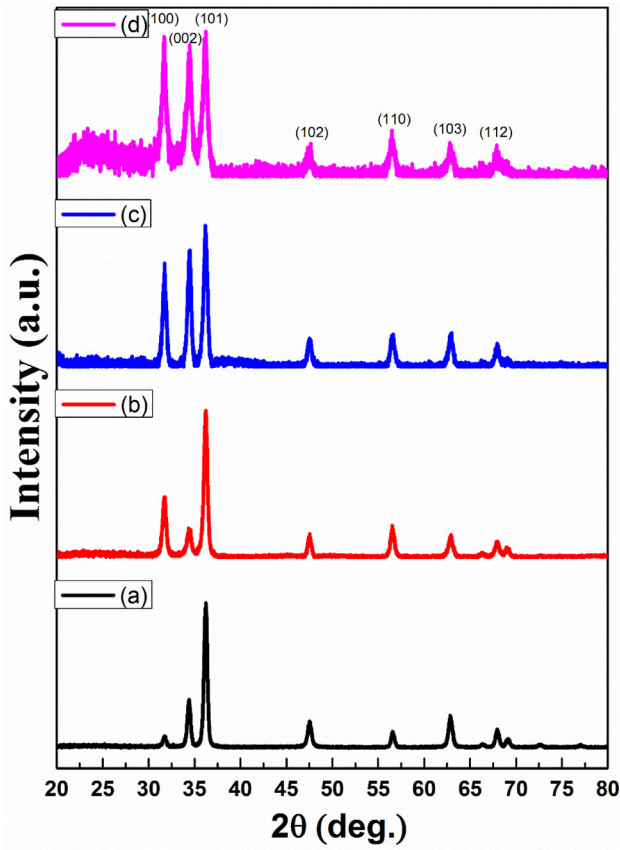


Fig. 3 XRD patterns of (a) undoped, (b) 5 wt%, (c) 10 wt%, and (d) 15 wt% IZO thin films

nanorods is reported by Kim et al. [41]. The grain boundaries hinder the electron flow since they act as potential barriers. In the presence of gas, the grain boundaries disappear and the resistance decreases which results in the high resistance modulation along the grain boundaries, thereby enhancing the performance of the sensing mechanism.

3.3 Photoluminescence studies

The PL spectra of the films were recorded at an excitation wavelength of 325 nm at ambient

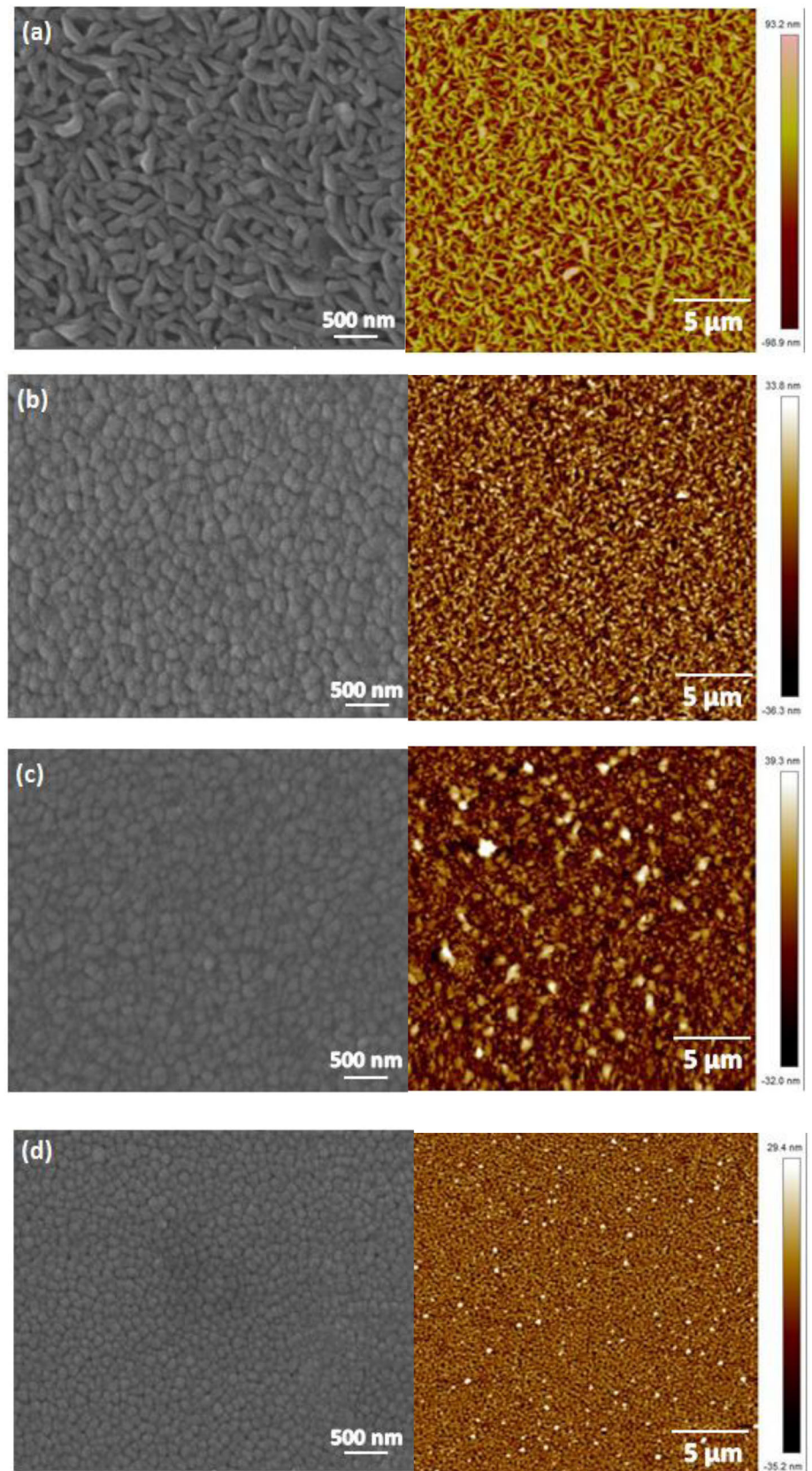
temperature [42]. The obtained spectra depict different emission centers in the ultraviolet region as well as in the visible region which are referred to as near band edge (NBE) emission and deep level emissions (DLE), respectively. Gaussian deconvolution of the PL spectra depicted in Fig. 5 identifies the distinct presence of different individual components which includes different emission centers. Table 2 shows the PL emission centers and the proposed origin of defects. The undoped ZnO films exhibit a strong NBE emission compared to the emission in the visible region. Emission in the visible region corresponds to the oxygen vacancy defects and interstitial defects in ZnO films [43]. The UV emission centered at 384 nm (3.23 eV) is originated from the free exciton recombination via exciton–exciton collision [43–45]. The blue emission centered at 476 nm (2.61 eV) and orange emission centered at 600 nm (2.07 eV) correspond to oxygen interstitial effects and green emission centered at 552 nm (2.25 eV) corresponds to oxygen vacancy defect (donor defect) since it acts as radiative centers in luminescence process [44, 45]. Figure 6 shows the PL band energy diagram with the proposed origin of defects.

Upon higher In doping concentration, it is observed that the different emission peaks are getting broadened which infers the enhancement of defect concentration. Doping with indium enhances the broadening of the NBE emission peak which implies the increase in exciton recombination [45]. It is observed that the orange and blue emissions get suppressed due to the quenching of oxygen interstitial defects. In 15 wt% In-doped ZnO film, a broadening of the green emission peak centered at 575 nm (2.16 eV) is observed which indicates the enhancement of oxygen vacancies. It is noteworthy that oxygen vacancies are inherent to ZnO thin films which are further observed to be enhanced upon In incorporation [44]. This characteristic of In: ZnO film

Table 1 Microstructural parameters of undoped and IZO thin films

Doping concentration (wt%)	FWHM (101) plane	Crystalline size, D (nm)	Dislocation density, δ (10^{15} lines m^{-2})	Strain, ϵ (10^{-3})
Undoped	0.42335	19.9	2.53	1.74
5	0.45803	18.5	2.93	1.88
10	0.50997	16.4	3.71	2.11
15	0.70102	13.1	5.79	2.63

Fig. 4 SEM and AFM micrographs of (a) undoped, (b) 5 wt%, (c) 10 wt%, and (d) 15 wt% IZO thin films



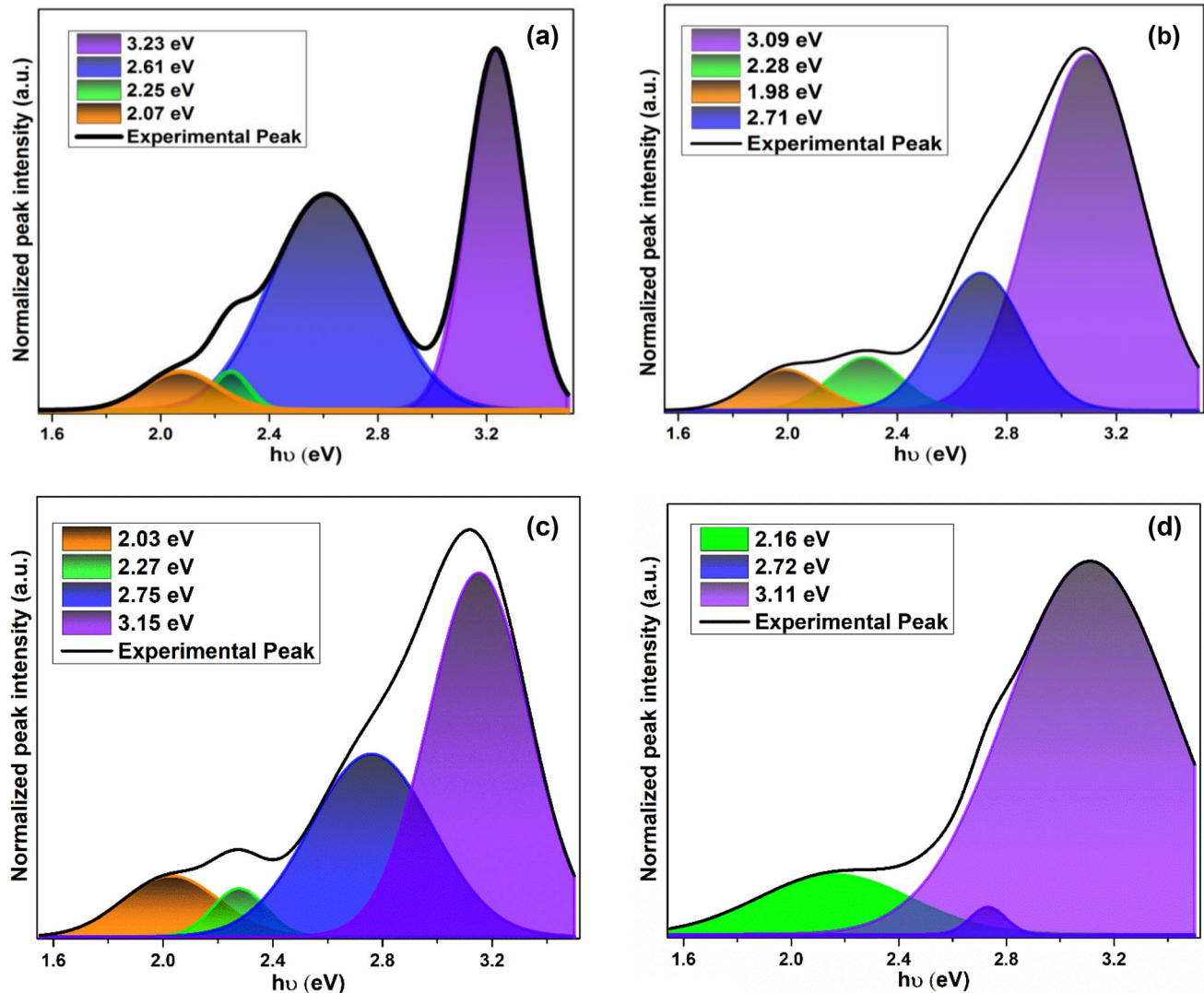


Fig. 5 Gaussian deconvoluted PL spectra of (a) undoped, (b) 5 wt%, (c) 10 wt%, and (d) 15 wt% IZO thin films

possesses a vital role in gas-sensing performance. The orange emission gets completely quenched and the blue emission at 456 nm (2.72 eV) gets suppressed in 15 wt% IZO film.

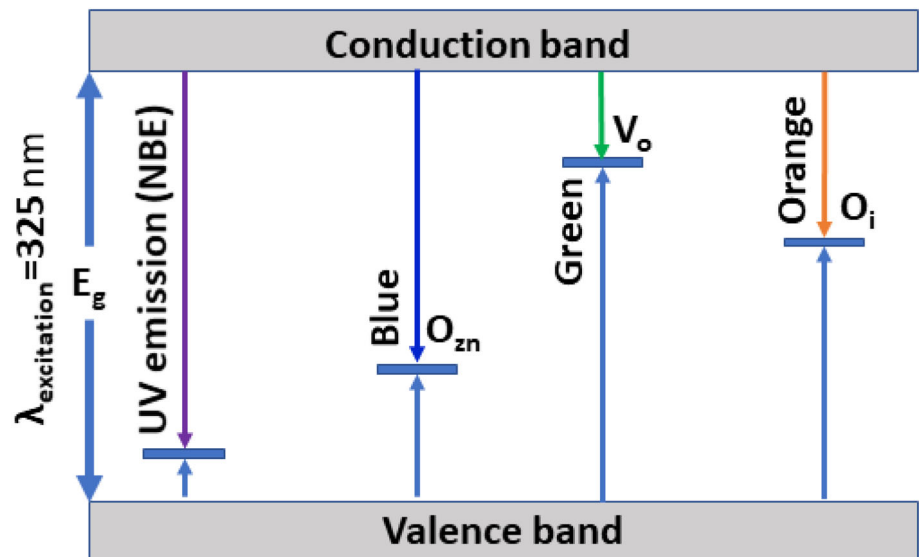
3.4 XPS studies

XPS studies were done to determine and verify the elemental composition of the undoped and IZO films. Carbon 1s binding energy at 284.5 eV was taken as the basis to correct the binding energies of the elements. The core-level spectra of Zn and O in both undoped and 15 wt% IZO thin films as well as the core-level spectra of In in 15 wt% IZO thin film are shown in Fig. 7a–c.

From the Zn core-level spectra of undoped film, the binding energies were observed at 1019 eV for the Zn 2p_{3/2} and 1042 eV for the Zn 2p_{1/2} peak. A minor shift in peak to higher binding energy values of 1022 eV for Zn 2p_{3/2} and 1045 eV for 2p_{1/2}, respectively, is observed from the core-level spectra of 15 wt% IZO thin film. The peak shift is attributed to the electronegative nature of In ($\chi = 1.78$) being higher than Zn ($\chi = 1.65$). Owing to the high electronegativity of indium, the free electron density of Zn in Zn–O–In bond of 15 wt% IZO film becomes lesser than Zn–O–Zn bond of undoped film. Accordingly, the screening effect of zinc gets weakened in IZO film and thereby increasing the Zn 2p binding energies. The Zn 2p_{3/2} and Zn 2p_{1/2} core-level peaks are per the binding energy confirming the Zn²⁺ oxidation

Table 2 PL emission centers and proposed origin of defects

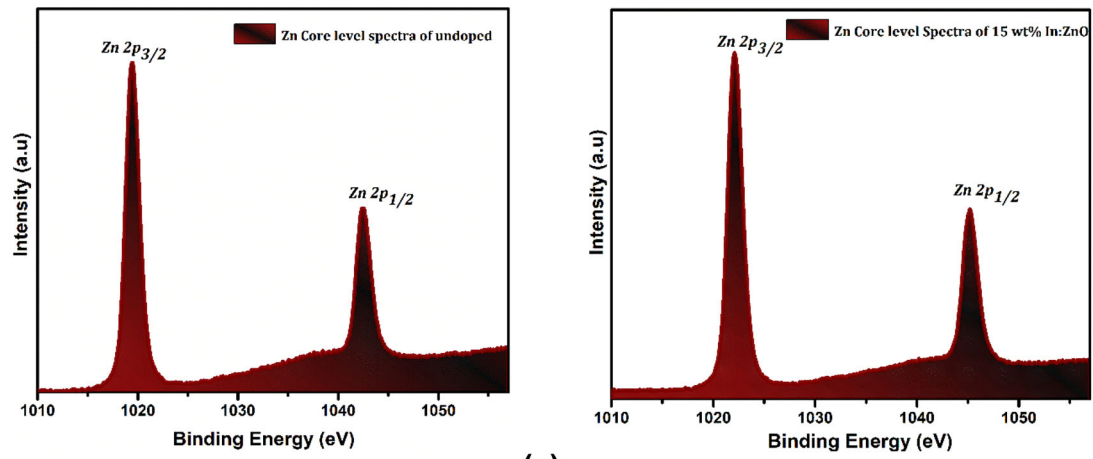
Doping concentration (wt%)	PL emission center (eV)	Color center	Proposed origin of defects
Undoped	3.23	UV	NBE emission
	2.61	Blue	Oxygen interstitial
	2.25	Green	Oxygen vacancy
	2.07	Orange	Oxygen interstitial
5	3.09	UV	NBE emission
	2.71	Blue	Oxygen interstitial
	2.28	Green	Oxygen vacancy
	1.98	Orange	Oxygen interstitial
10	3.15	UV	NBE emission
	2.75	Blue	Oxygen interstitial
	2.27	Green	Oxygen vacancy
	2.03	Orange	Oxygen interstitial
15	3.11	UV	NBE emission
	2.72	Blue	Oxygen interstitial
	2.16	Green	Oxygen vacancy

Fig. 6 Schematic of the band diagram of PL emission

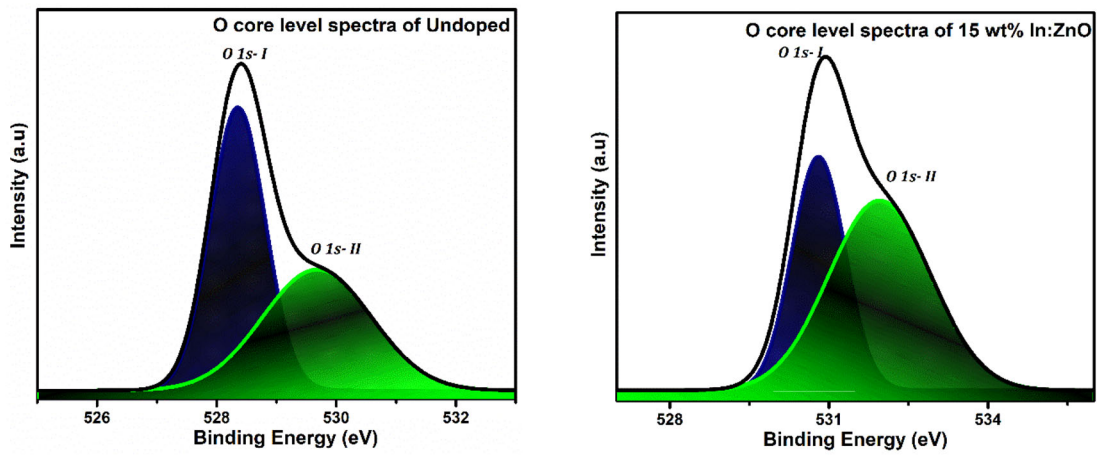
state, thereby approving the stability of the oxidation state of Zn element with indium incorporation [46–48].

The Gaussian function was utilized to deconvolute the core-level spectra of O 1s peaks into integral components and was deconvoluted into two peaks, namely O 1s-I and O 1s-II at binding energies of 528.3 eV and 529.7 eV, respectively. The peak at 528.3 eV is related to O^{2-} ions combined with Zn atom and the peak at 529.7 eV to oxygen deficiency or vacancy defect. A slight shift in binding energies to 530.7 eV for O 1s-I and 531.9 eV for O 1s-II is observed in 15 wt% IZO thin film owing to the reason mentioned above in the case of Zn 2p peak shift. The

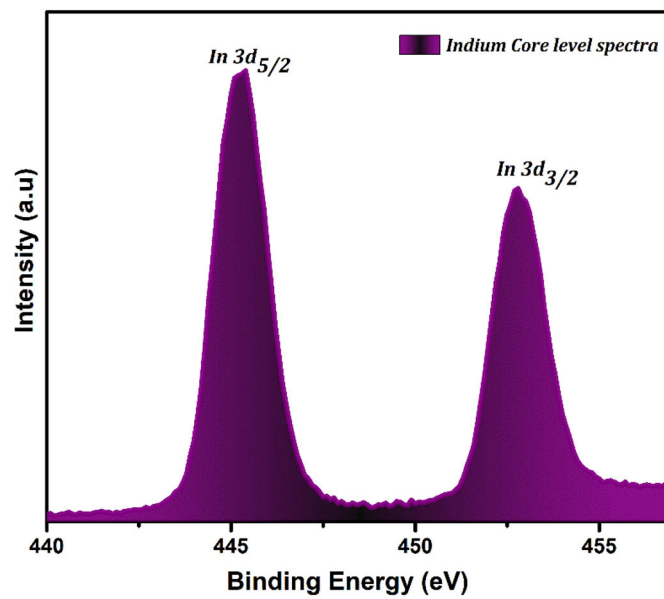
area ratios of O 1s-I and O 1s-II peaks are obtained by $(O\ 1s-I)/(O\ 1s-I + O\ 1s-II)$ and $(O\ 1s-II)/(O\ 1s-I + O\ 1s-II)$, respectively. In the undoped ZnO film, the area ratios are $\sim 54.02\%$ and $\sim 45.98\%$ for O 1s-I and O 1s-II peaks, respectively. The incorporation of 15 wt% indium changes the ratios of the O 1s-I and O 1s-II peaks to 38.82% and 61.18%, respectively, suggesting the enhancement of oxygen vacancy-related defects upon doping with indium. This observation reveals that the indium incorporation into ZnO lattice can enhance the CO gas-sensing performance as oxygen vacancies serve as an active adsorption site for the gas species [46–48].



(a)



(b)



(c)

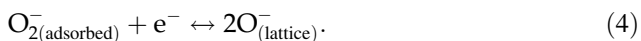
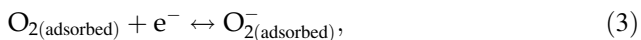
◀ **Fig. 7** (a) Zn core-level spectra of undoped and 15 wt% IZO thin films, (b) O core-level spectra of undoped and 15 wt% IZO thin films, (c) In core-level spectra of 15 wt% IZO thin films

The results of the In 3d core region reveal the presence of doublet peaks that correspond to In 3d_{3/2} and In 3d_{5/2} peaks at 452.8 eV and 445.3 eV, respectively, which confirm the +3 oxidation state of indium, thereby indicating the effective incorporation of indium to the ZnO lattice. No phases of In₂O₃ are found which is in line with the XRD studies [46, 48–51].

3.5 Gas sensing studies

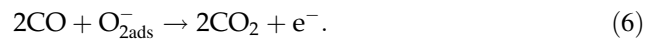
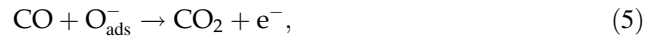
Gas adsorption by the sensing layer is strongly reliant on the thermally activated diffusion process. Therefore, the sensing performance is dependent on the operating temperature [41]. The operating temperature was optimized to be 300 °C and the sensing voltage was found to be 1 V. Below 300 °C, the sensor does not have adequate energy for the adsorption of CO molecules [26].

Since CO is a type of reducing gas [52] and the IZO layer exists as an n-type semiconductor [53], the sensor resistance reduces upon gas exposure. When synthetic air is flown to the chamber where the ZnO sensor is placed, the oxygen because of its high electron affinity around 0.43 eV gets readily adsorbed to the sensor surface [15, 54]. The adsorbed oxygen extracts electrons present in the conduction band and gets converted into oxygen ion (O₂⁻, O⁻ and O²⁻) by the following reactions [55]:



As a result, a layer of depleted electrons is formed, also called a space charge layer which creates a potential barrier between adjacent grains. This layer is a space of high resistance or low current since electrons get obstructed from motion due to the barrier height. Stabilization of sensor resistance occurs when the adsorbed oxygen species gets saturated. Exposure to CO gas causes the electrons to be free to move back to the ZnO on reaction with the chemisorbed oxygen, thereby reducing the width of the space charge region which in sequence decreases the resistance. The gas molecules consume the

oxygen ions adsorbed which cause a variation in the density of oxygen ions and result in a change in the electrical resistance. The surface reactions on exposure to CO gas is given by [5].



The sensor resistance reaches the saturation level when the adsorbed oxygen gets entirely reacted with the CO gas. The schematic representing the mechanism of CO gas sensing by the ZnO-sensing layer is shown in Fig. 8.

Figure 9 depicts the dynamic response curves of the undoped and IZO films. The response time and recovery time of the In-doped ZnO sensors toward various concentrations of CO gas are specified in Table 3. The response and recovery time are the most significant characteristics of a sensor. The undoped sensor displayed a response time of 76 s toward 1 ppm of gas and 120 s toward 5 ppm of gas. From the response curve analysis, it is evident that the 15 wt% sample had a substantial effect on the response time as it could detect the lowest ppm of CO gas (1 ppm) with a quick response time of 56 s. It showed a response time of 24 s toward 5 ppm of CO gas. Therefore, 15 wt% In doping exhibited quick response time for the CO gas-sensing performance. It has a high surface to volume ratio and large grain boundaries compared to other films which are evident from SEM and XRD analysis. The presence of oxygen vacancies confirmed from PL and XPS studies contributes to the sensing performance as it provides more sites for oxygen adsorption [56]. The trivalency state of In³⁺ compels to create more oxygen vacancy by weakening the metal–oxygen bond energy to conserve the charge neutrality in ZnO lattice. This could be complemented by the fact that In–O bonding energy is lower than Zn–O bonding energy [57, 58]. More the number of vacant sites, more the adsorption of oxygen ions which enhances the number of CO gas species reacting, thereby increasing the sensor response. Sumati et al. [59] confirmed an excellent relation between CO gas-sensing response and the oxygen vacancy defect. They reported the significance of oxygen vacancies in controlling the CO-sensing features of ZnO. The adsorption of oxygen thickens the depletion region which provides active sites for the CO gas adsorption [60–62]. Al-Hashem et al. [63] defined oxygen

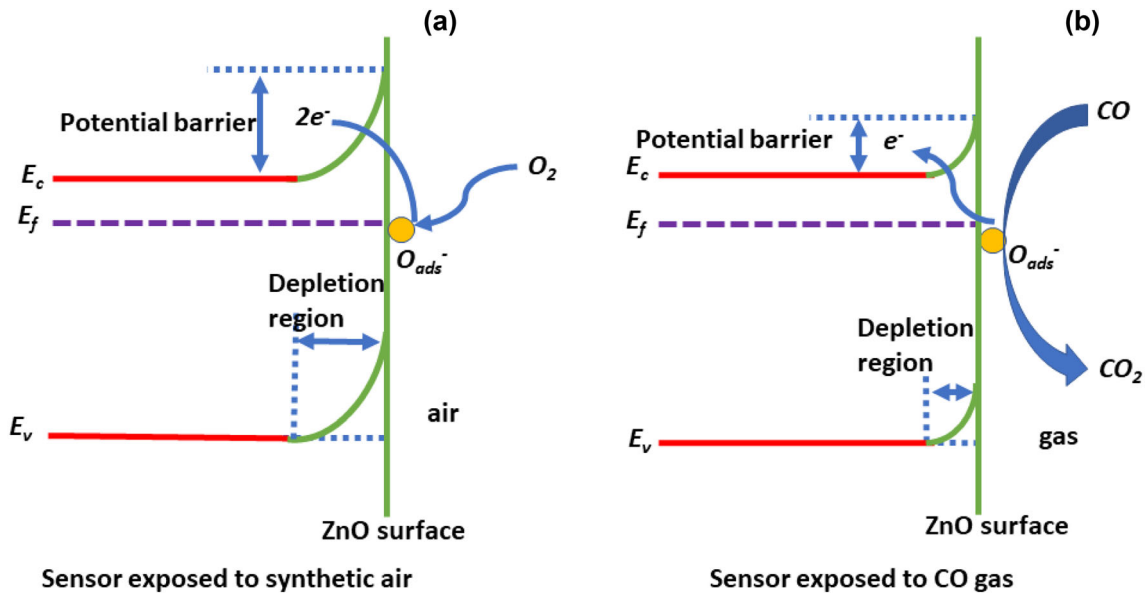


Fig. 8 Illustration of CO gas sensing by ZnO layer in (a) air and (b) CO gas

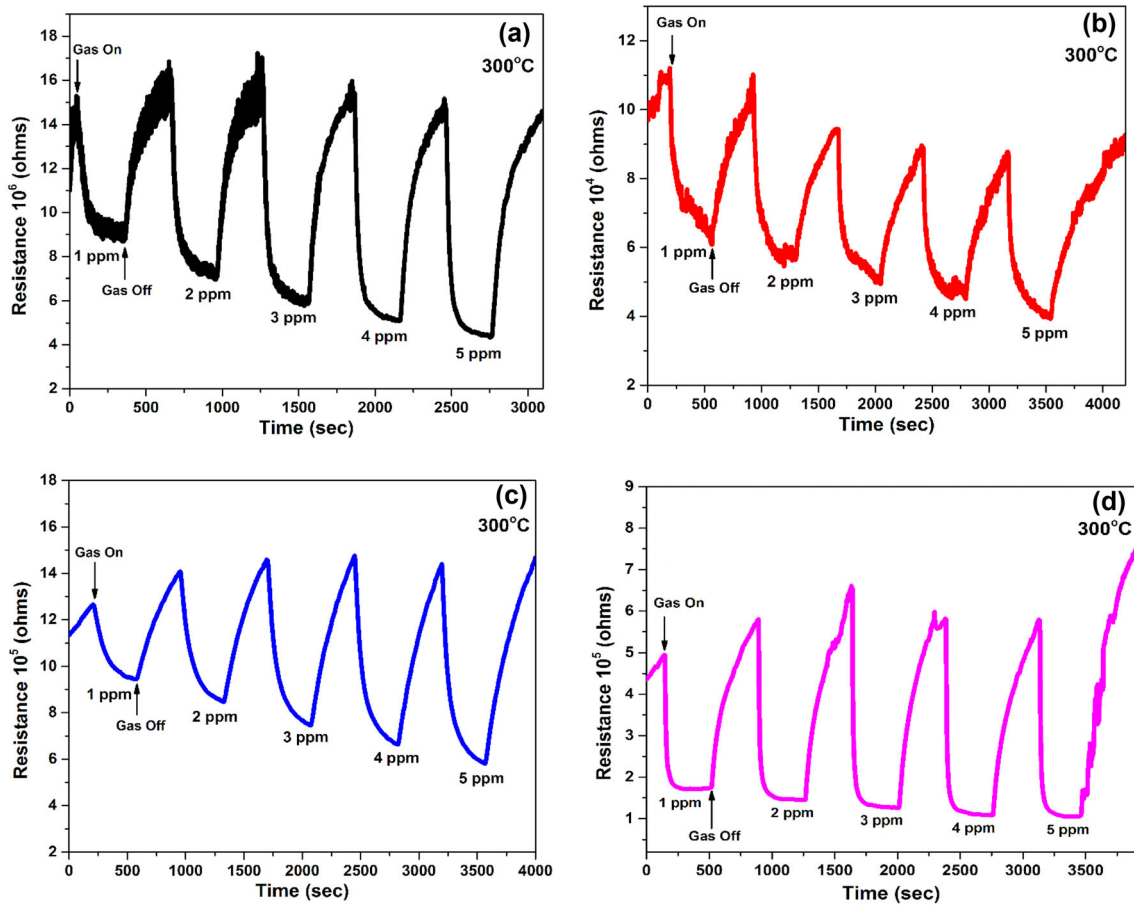


Fig. 9 Dynamic response plots of (a) undoped, (b) 5 wt%, (c) 10 wt%, and (d) 15 wt% IZO thin films

Table 3 Response and recovery times to different CO concentrations of undoped and IZO sensors

Gas concentration/In concentration (ppm)	Response time (s)				Recovery time (s)			
	Undoped	5 wt%	10 wt%	15 wt%	Undoped	5 wt%	10 wt%	15 wt%
1	77	238	230	56	173	313	315	275
2	121	160	236	102	120	294	320	38
3	102	250	221	100	184	302	299	48
4	134	130	232	126	190	313	318	15
5	120	235	246	24	232	236	314	273

vacancy as a critical defect for the gas-sensing mechanism. Oxygen vacancies increase the surface-adsorbed oxygen concentration complementing the modification of baseline resistance of the sensor.

The sensor response calculated using the formula [56] versus In concentration for various CO gas concentrations is shown in Fig. 10 as well as tabulated in Table 4.

$$\text{Response} = (R_a - R_g) / R_g, \quad (7)$$

where R_g and R_a denote resistance in target gas and resistance in air, respectively. CO gas-sensing studies indicate that 15 wt% of IZO thin film exhibits high response almost two times (1.84) to a low concentration of the gas (1 ppm) at 300 °C compared to undoped (0.53). The sensor response with different CO gas concentrations for various In doping concentrations is shown in Fig. 11.

The high response and quick response times of 15 wt% IZO sensor can be correlated (i) to the creation of

higher defects concerning the oxygen vacancies providing supplementary active adsorption sites for CO gas adsorption and (ii) to the large number of well-defined grain boundaries catalyzed by indium which indicates large surface to volume ratio, thus enhancing the adsorption of CO gas species [35].

Selectivity is a significant property of a gas sensor from a practical standpoint. The optimized sensor (15 wt% In:ZnO) was exposed to 3 ppm of carbon monoxide (CO), hydrogen sulfide (H₂S), sulfur dioxide (SO₂), and nitrogen dioxide (NO₂) at 300 °C. The sensor showed an enhanced response toward CO gas than the other tested gases, thereby confirming an excellent selectivity toward the desired CO gas. Figure 12 shows the histogram of selectivity of 15 wt% IZO sensor toward 3 ppm of CO, SO₂, H₂S, and NO₂ gases at 300 °C.

The sensor stability is tested after 1 year. The dynamic response curve of the freshly prepared film and the film aged/preserved for 1 year of 15 wt% IZO is shown in Fig. 13 and the calibration curve is shown in Fig. 14. After 1 year, the sensor response reduced slightly by 13% to 1 ppm of CO gas concentration confirming the long-term stability of the sensor.

A comparison study of the CO-sensing characteristics of IZO material with other recent studies of CO gas sensors based on ZnO synthesized via various methods is done and presented in Table 5. Most of the work represented the lowest detection limit of 5 ppm and the optimum detection was in the range of 1000 ppm. Our work reports the detection of the lowest concentration of 1 ppm of CO gas with In-doped ZnO gas sensor.

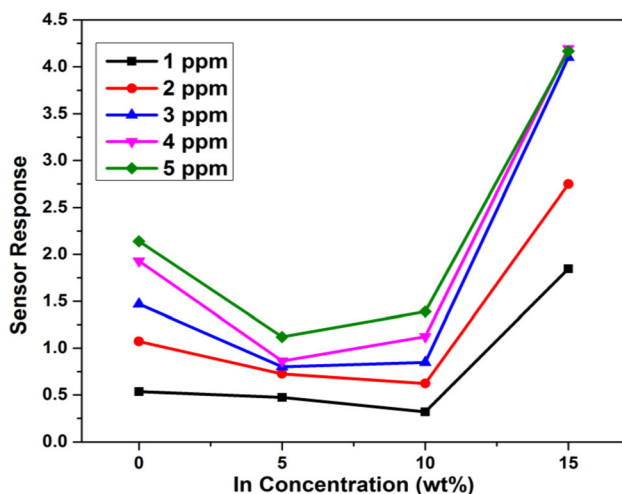
**Fig. 10** Sensor response versus In concentration for different concentrations of CO gas

Table 4 Sensor response values of undoped and IZO layers toward different concentrations of CO gas

Gas concentration/In concentration (ppm)	Sensor response			
	Undoped	5 wt%	10 wt%	15 wt%
1	0.53	0.47	0.32	1.84
2	1.07	0.72	0.62	2.75
3	1.47	0.80	0.85	4.10
4	1.93	0.86	1.12	4.19
5	2.14	1.12	1.39	4.17

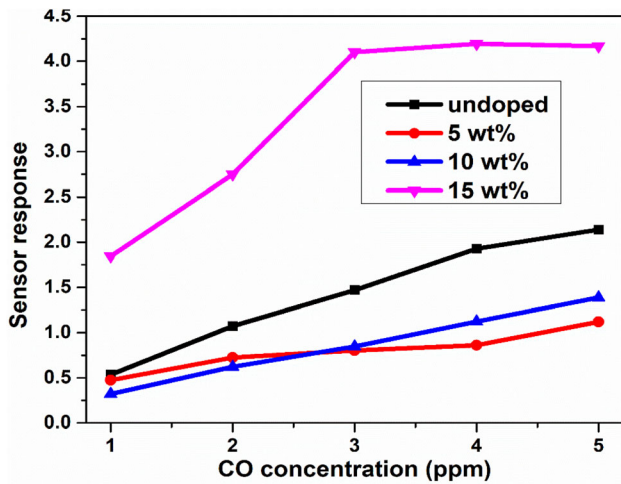


Fig. 11 Sensor response versus CO concentration for different indium doping concentrations

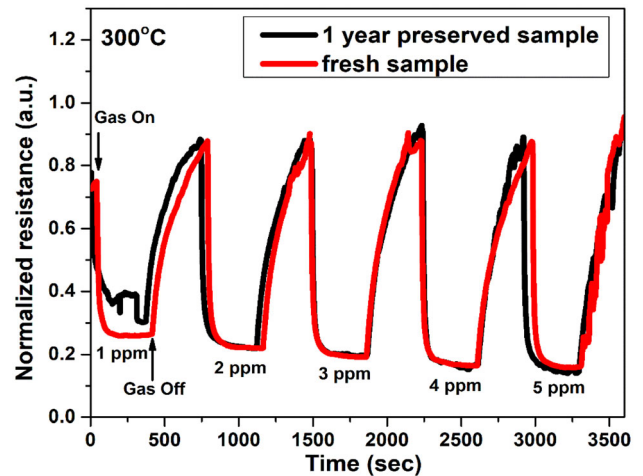


Fig. 13 Dynamic response curve of 1 year preserved and fresh samples of 15 wt% IZO

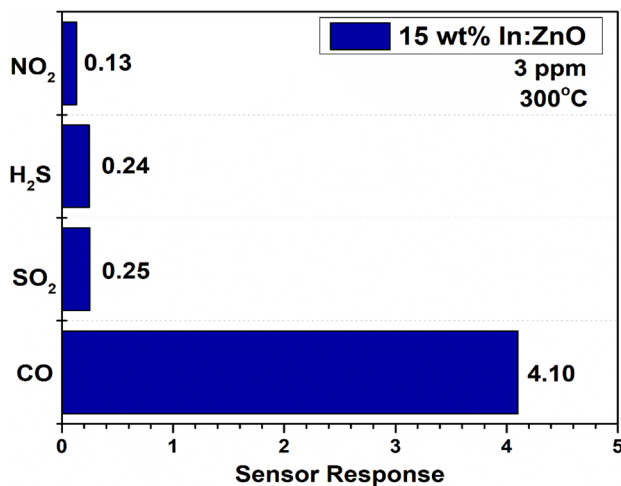


Fig. 12 Histogram of selectivity of 15 wt% IZO sensor toward 3 ppm of CO, SO₂, H₂S, and NO₂ gases at 300 °C

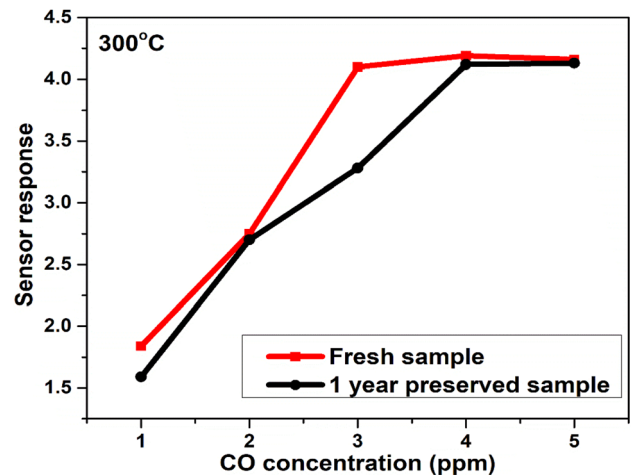


Fig. 14 Calibration curve corresponding to Fig. 13

4 Conclusion

Undoped, 5 wt%, 10 wt%, and 15 wt% IZO thin films are synthesized via chemical spray technique. The films are characterized mainly by XRD, AFM, SEM,

PL, and XPS to confirm the structural, morphological, and defect properties to understand the sensing mechanism. The role of In doping in ZnO nanostructures in CO gas-sensing was carried out with different doping concentrations. It is observed that 15

Table 5 Comparison table with previously reported ZnO-based CO gas sensor

Material	Preparation method	Concentration (ppm)	Operating temperature (°C)	Response time (s)	Recovery time (s)	Sensor response	References
In:ZnO thin films	Spray pyrolysis	5 (LDL: 1)	300	24 56 (1 ppm)	273 275 (1 ppm)	4.17 1.84 (1 ppm)	This work
In:ZnO nanoparticles	Sol-gel	50 (LDL: 5)	300	~ 20	~ 45	3.5	[28]
In:ZnO nanoparticles	Sol-gel	50 (LDL: 5)	300	NA	NA	4.80	[26]
Al:ZnO nanoparticles	Sol-gel	50 (LDL: 5)	300	7	16–30 s	1.6	[25]
ZnO honeycomb	RF sputtering	3	300	180	210	81.2	[64]
ZnO:rGO nanoparticles	Hydrothermal	1000	200	7	9	85.2	[65]
Pd:ZnO nanostructures	RF sputtering	50	150	17	23	1022	[66]
Cu:ZnO	Co-sputtering	20	350	NA	NA	2.7	[67]

LDL lowest detection limit, NA not applicable

wt% indium doping enhanced the sensing performance effectively at a low concentration of 1 ppm of the CO gas as well as at 5 ppm for an optimum operating temperature of 300 °C. High response and quick response times were obtained for the 15 wt% IZO sensor that are attributed to the oxygen vacancies present in it. Excellent selectivity among other tested gases and long-term stability were exhibited by the sensor which are crucial parameters from a practical standpoint. Thus, indium proved to be a promising dopant to ZnO nanostructures for CO gas sensor applications.

Funding

Open access funding provided by Manipal Academy of Higher Education, Manipal.

Declarations

Conflict of interest The authors declare that they have no conflict of interest.

Open Access This article is licensed under a Creative Commons Attribution 4.0 International License, which permits use, sharing, adaptation, distribution and reproduction in any medium or format, as long as you give appropriate credit to the original author(s) and the source, provide a link to the Creative Commons licence, and indicate if changes were made. The images or other third party material in this article are included in the article's Creative Commons licence, unless indicated otherwise in a credit line to the material. If material is not included in the article's Creative Commons licence and your intended use is not permitted by statutory regulation or exceeds the permitted use, you will need to obtain permission directly from the copyright holder. To view a copy of this licence, visit <http://creativecommons.org/licenses/by/4.0/>.

Supplementary Information: The online version contains supplementary material available at <http://doi.org/10.1007/s10854-021-06745-1>.

References

1. Y.J. Onofre, A.C. Catto, S. Bernardini, T. Fiorido, K. Aguir, E. Longo, V.R. Mastelaro, L.F. da Silva, M.P.F. de Godoy, Highly selective ozone gas sensor based on nanocrystalline Zn_{0.95}Co_{0.05}O thin film obtained via spray pyrolysis technique. *Appl. Surf. Sci.* **478**, 347–354 (2019). <https://doi.org/10.1016/j.apsusc.2019.01.197>
2. Z. El Khalidi, E. Comini, B. Hartiti, A. Moumen, H.M. Arachchige, S. Fadili, P. Thevenin, A. Kamal, Effect of vanadium doping on ZnO sensing properties synthesized by spray pyrolysis. *Mater. Des.* **139**, 56–64 (2018). <https://doi.org/10.1016/j.matdes.2017.10.074>
3. R.D. Ladhe, P.K. Baviskar, S.M. Pawar, J.H. Kim, B.R. Sankapal, The *n*-Bi₂S₃/*p*-PbS heterojunction for room temperature LPG sensors. *Sens. Actuators A* **267**, 187–193 (2017). <https://doi.org/10.1016/j.sna.2017.10.024>
4. Q. Wang, C. Wang, H. Sun, P. Sun, Y. Wang, J. Lin, G. Lu, Microwave assisted synthesis of hierarchical Pd/SnO₂ nanostructure for CO gas sensor. *Sens. Actuators B* **222**, 257–263 (2016). <https://doi.org/10.1016/j.snb.2015.07.115>
5. Z. Li, H. Li, Z. Wu, M. Wang, J. Luo, H. Torun, P.A. Hu, C. Yang, M. Grundmann, X. Liu, Y.Q. Fu, Advances in designs and mechanisms of semiconducting metal oxide nanostructures for high-precision gas sensors operated at room temperature. *Mater. Horiz.* **6**, 470 (2019). <https://doi.org/10.1039/c8mh01365a>
6. J. Dang, H. Yu, Y. Sun, Y. Wang, A CO trace gas detection system based on continuous wave DFB-QCL. *Infrared Phys. Technol.* **82**, 183–191 (2017). <https://doi.org/10.1016/j.infrared.2016.12.012>
7. A. Mirzaei, S. Park, G.-J. Sun, H. Kheel, C. Lee, CO sensing properties of In₄Sn₃O₁₂ and TeO₂ composite nanoparticle sensors. *J. Hazard. Mater.* **305**, 130–138 (2016). <https://doi.org/10.1016/j.jhazmat.2015.11.044>
8. J.-H. Kim, A. Mirzaei, H.W. Kim, S.S. Kim, Extremely sensitive and selective sub-ppm CO detection by the synergistic effect of Au nanoparticles and core-shell nanowires. *Sens. Actuators B* **249**, 177–188 (2017). <https://doi.org/10.1016/j.snb.2017.04.090>
9. J.M.G. Leano, J.M.L.A. Villapando, A.E. Balaaldia, G. Gianan, F.K.B. Manalo, E.A. Florido, Carbon monoxide gas sensing using zinc oxide film deposited by spray pyrolysis. *IOP Conf. Ser. Mater. Sci. Eng.* **201**, 012051 (2017). <https://doi.org/10.1088/1757-899X/201/1/012051>
10. T. Meredith, A. Vale, Carbon monoxide poisoning. *Br. Med. J.* **296**(1988), 77–79 (1988). <https://doi.org/10.1136/bmj.296.6615.77>
11. R.M. Hall, G. Scott Earnest, D.R. Hammond, K.H. Dunn, A. Garcia, A summary of research and progress on carbon monoxide exposure control solutions on houseboats. *J. Occup. Environ. Hyg.* **11**, D92–D100 (2014). <https://doi.org/10.1080/15459624.2014.895374>
12. J. Zhang, Z. Qin, D. Zeng, C. Xie, Metal-oxide-semiconductor based gas sensors: screening, preparation, and integration. *Phys. Chem. Chem. Phys.* **19**, 6313 (2017). <https://doi.org/10.1039/c6cp07799d>
13. M. Kumar, B. Singh, P. Yadav, V. Bhatt, M. Kumar, K. Singh, A.C. Abhyankar, A. Kumar, J.-H. Yun, Effect of structural defects, surface roughness on sensing properties of Al doped ZnO thin films deposited by chemical spray pyrolysis technique. *Ceram. Int.* **43**, 3562–3568 (2017). <https://doi.org/10.1016/j.ceramint.2016.11.191>
14. Q. Zhou, W. Zeng, W. Chen, L. Xu, R. Kumar, A. Umar, High sensitive and low-concentration sulfur dioxide (SO₂) gas sensor application of heterostructure NiO–ZnO nanodisks. *Sens. Actuators B* **298**, 126870 (2019). <https://doi.org/10.1016/j.snb.2019.126870>
15. Y.-F. Sun, S.-B. Liu, F.-L. Meng, J.-Y. Liu, Z. Jin, L.-T. Kong, J.-H. Liu, Metal oxide nanostructures and their gas sensing properties: a review. *Sensors* **12**, 2610–2631 (2012). <https://doi.org/10.3390/s120302610>
16. R. Ahmad, S.M. Majhi, X. Zhang, T.M. Swager, K.N. Salama, Recent progress and perspectives of gas sensors based on vertically oriented ZnO nanomaterials. *Adv. Colloid Interface Sci.* **270**, 1–27 (2019). <https://doi.org/10.1016/j.cis.2019.05.006>
17. A. Mirzaei, J.-H. Kim, H.W. Kim, S.S. Kim, Resistive-based gas sensors for detection of benzene, toluene and xylene (BTX) gases: a review. *J. Mater. Chem. C* **6**, 4342–4370 (2018). <https://doi.org/10.1039/C8TC00245B>
18. M. Sinha, R. Mahapatra, B. Mondal, T. Maruyama, R. Ghosh, Ultra-fast and reversible gas sensing properties of ZnO nanowire arrays grown by hydrothermal technique. *J. Phys. Chem. C* **120**, 3019–3025 (2016). <https://doi.org/10.1021/acs.jpcc.5b11012>
19. S.J. Patil, A.V. Patil, C.G. Dighavkar, K.S. Thakare, R.Y. Borase, S.J. Nandre, N.G. Deshpande, R.R. Ahire, Semiconductor metal oxide compounds based gas sensors: a literature review. *Front. Mater. Sci.* **9**, 14–37 (2015). <https://doi.org/10.1007/s11706-015-0279-7>
20. V. Najafi, S. Zolghadr, S. Kimiagar, Remarkable reproducibility and significant sensitivity of ZnO nanoparticles covered by chromium(III) oxide as a hydrogen sulfide gas sensor. *Optik* **182**, 249–256 (2019). <https://doi.org/10.1016/j.ijleo.2019.01.015>
21. V. Galstyan, E. Comini, C. Baratto, G. Faglia, G. Sberveglieri, Nanostructured ZnO chemical gas sensors. *Ceram. Int.* **41**, 14239–14244 (2015). <https://doi.org/10.1016/j.ceramint.2015.07.052>

22. M. Kumar, V.S. Bhati, S. Ranwa, J. Singh, M. Kumar, Pd/ZnO nanorods based sensor for highly selective detection of extremely low concentration hydrogen. *Sci. Rep.* **7**, 236 (2017). <https://doi.org/10.1038/s41598-017-00362-x>
23. V.L. Patil, S.A. Vanalakar, P.S. Patil, J.H. Kim, Fabrication of nanostructured ZnO thin films based NO₂ gas sensor via SILAR technique. *Sens. Actuators B* **239**, 1185–1193 (2017). <https://doi.org/10.1016/j.snb.2016.08.130>
24. M. Mehedi Hassan, W. Khan, P. Mishra, S.S. Islam, A.H. Naqvi, Enhancement of the alcohol gas sensitivity in Cr doped ZnO gas sensor. *Mater. Res. Bull.* **93**, 391–400 (2017). <https://doi.org/10.1016/j.materresbull.2017.05.019>
25. M. Hjiri, L. El Mir, S.G. Leonardi, A. Pistone, L. Mavilia, G. Neri, Al-doped ZnO for highly sensitive CO gas sensors. *Sens. Actuators B* **196**, 413–420 (2014). <https://doi.org/10.1016/j.snb.2014.01.068>
26. M. Hjiri, R. Dhahri, K. Omri, L. El Mir, S.G. Leonardi, N. Donato, G. Neri, Effect of indium doping on ZnO based-gas sensor for CO. *Mater. Sci. Semicond. Process.* **27**, 319–325 (2014). <https://doi.org/10.1016/j.mssp.2014.07.009>
27. M. Hjiri, L. El Mir, S.G. Leonardi, N. Donato, G. Neri, CO and NO₂ selective monitoring by ZnO-based sensors. *Nanomaterials* **3**, 357–369 (2013). <https://doi.org/10.3390/na3030357>
28. R. Dhahri, M. Hjiri, L. El Mir, H. Alamri, A. Bonavita, D. Iannazzo, S.G. Leonardi, G. Neri, CO sensing characteristics of In-doped ZnO semiconductor nanoparticles. *J. Sci. Adv. Mater. Devices* **2**, 34–40 (2017). <https://doi.org/10.1016/j.jsamd.2017.01.003>
29. X. Pan, X. Zhao, Ultra-high sensitivity zinc oxide nanocombs for on-chip room temperature carbon monoxide sensing. *Sensors* **15**, 8919–8930 (2015). <https://doi.org/10.3390/s150408919>
30. A. Paliwal, A. Sharma, M. Tomar, V. Gupta, Carbon monoxide (CO) optical gas sensor based on ZnO thin films. *Sens. Actuators B* **250**, 679–685 (2017). <https://doi.org/10.1016/j.snb.2017.05.064>
31. J. Leng, Z. Wang, J. Wang, H.-H. Wu, G. Yan, X. Li, H. Guo, Y. Liu, Q. Zhang, Z. Guo, Advances in nanostructures fabricated via spray pyrolysis and their applications in energy storage and conversion. *Chem. Soc. Rev.* **48**, 3015 (2019). <https://doi.org/10.1039/c8cs00904j>
32. R. Biswal, A. Maldonado, J. Vega-Pérez, D.R. Acosta, M. De La Luz Olvera, Indium doped zinc oxide thin films deposited by ultrasonic chemical spray technique, starting from zinc acetylacetonate and indium chloride, *Materials* **7**, 5038–5046 (2014). <https://doi.org/10.3390/ma7075038>
33. M.S. Tokumoto, A. Smith, C.V. Santilli, S.H. Pulcinelli, E. Elkaim, V. Briois, Effect of In concentration in the starting solution on the structural and electrical properties of ZnO films prepared by the pyrosol process at 450°C. *J. Non-cryst. Solids* **273**, 302–306 (2000). [https://doi.org/10.1016/S0022-3093\(00\)00176-9](https://doi.org/10.1016/S0022-3093(00)00176-9)
34. C.H. Tan, S.T. Tan, H.B. Lee, R.T. Ginting, H.F. Oleiwi, C.C. Yap, M.H.H. Jumali, M. Yahaya, Automated room temperature optical absorbance CO sensor based on In-doped ZnO nanorod. *Sens. Actuators B* **248**, 140–152 (2017). <https://doi.org/10.1016/j.snb.2017.02.161>
35. B. Soltabayev, M.A. Yildirim, A. Ates, S. Acar, The effect of indium doping concentration on structural, morphological and gas sensing properties of IZO thin films deposited SILAR method. *Mater. Sci. Semicond. Process.* **101**, 28–36 (2019). <https://doi.org/10.1016/j.mssp.2019.05.026>
36. T.-H. Fang, S.-H. Kang, Effect of indium dopant on surface and mechanical characteristics of ZnO: In nanostructured films. *J. Phys. D* **41**, 245303 (2008). <https://doi.org/10.1088/0022-3727/41/24/245303>
37. R.K. Gupta, K. Ghosh, R. Patel, S.R. Mishra, P.K. Kahol, Band gap engineering of ZnO thin films by In₂O₃ incorporation. *J. Cryst. Growth* **310**, 3019–3023 (2008). <https://doi.org/10.1016/j.jcrysgro.2008.03.004>
38. L.K. Dintle, P.V.C. Luhanga, C. Moditswe, C.M. Muiva, Compositional dependence of optical and electrical properties of indium doped zinc oxide (IZO) thin films deposited by chemical spray pyrolysis. *Physica E* **99**, 91–97 (2018). <https://doi.org/10.1016/j.physe.2018.01.009>
39. A. Antony, S. Pramodini, P. Poornesh, I.V. Kityk, A.O. Fedorchuk, G. Sanjeev, Influence of electron beam irradiation on non linear optical properties of Al doped ZnO thin films for optoelectronic device applications in the CW laser regime. *Opt. Mater.* **62**, 64–71 (2016). <https://doi.org/10.1016/j.optmat.2016.09.053>
40. H.W. Kim, Y.J. Kwon, A. Mirzaei, S.Y. Kang, M.S. Choi, J.H. Bang, S.S. Kim, Synthesis of zinc oxide semiconductors–graphene nanocomposites by microwave irradiation for application to gas sensors. *Sens. Actuators B* **249**, 590–601 (2017). <https://doi.org/10.1016/j.snb.2017.03.149>
41. J.-H. Kim, A. Mirzaei, H.W. Kim, P. Wu, S.S. Kim, Design of supersensitive and selective ZnO-nanofiber-based sensors for H₂ gas sensing by electron-beam irradiation. *Sens. Actuators B* **293**, 210–223 (2019). <https://doi.org/10.1016/j.snb.2019.04.113>
42. A. Antony, P. Poornesh, I.V. Kityk, G. Myronchuk, G. Sanjeev, V.C. Petwal, V.P. Verma, J. Dwivedi, A study of 8 MeV e-beam on localized defect states in ZnO nanostructures and its role on photoluminescence and third harmonic generation. *J. Lumin.* **207**, 321–332 (2019). <https://doi.org/10.1016/j.jlumin.2018.11.043>
43. A.B. Djuricic, Y.H. Leung, K.H. Tam, Green, yellow and orange defect emissions from ZnO nanostructures: Influence

- of excitation wavelength. *Appl. Phys. Lett.* **88**, 103107 (2006). <https://doi.org/10.1063/1.2182096>
44. A.B. Djuriscic, Y.H. Leung, K.H. Tam, Y.F. Hsu, L. Ding, W.K. Ge, Y.C. Zhong, K.S. Wong, W.K. Chan, H.L. Tam, K.W. Cheah, W.M. Kwok, D.L. Phillips, Defect emissions in ZnO nanostructures. *Nanotechnology* **18**, 095702 (2007). <https://doi.org/10.1088/0957-4484/18/9/095702>
45. M. Benhaliliba, C.E. Benouis, M.S. Aida, F. Yakuphanoglu, A. Sanchez Juarez, Indium and aluminium-doped ZnO thin films deposited onto FTO substrates: nanostructure, optical, photoluminescence and electrical properties. *J. Sol–Gel Sci. Technol.* **55**, 335–342 (2010). <https://doi.org/10.1007/s10971-010-2258-x>
46. Z. Zhu, B. Li, J. Wen, Z. Chen, Z. Chen, R. Zhang, S. Ye, G. Fang, J. Qian, Indium-doped ZnO horizontal nanorods for high on-current field effect transistors. *RSC Adv.* **7**, 54928 (2017). <https://doi.org/10.1039/c7ra09105b>
47. W. Zhao, H. Li, Z. Liu, D. Wang, S.F. Liu, Controlled defects and enhanced electronic extraction in fluorine incorporated zinc oxide for high performance planar perovskite solar cells. *Sol. Energy Mater. Sol. Cells* **182**, 263–271 (2018). <https://doi.org/10.1016/j.solmat.2018.03.047>
48. A. Antony, P. Poornesh, K. Ozga, P. Rakus, A. Wojciechowski, I.V. Kityk, G. Sanjeev, V.C. Petwal, V.P. Verma, J. Dwivedi, An electron beam induced study in fluorine doped ZnO nanostructures for optical filtering and frequency conversion application. *Opt. Laser Technol.* **115**, 519–530 (2019). <https://doi.org/10.1016/j.optlastec.2019.03.003>
49. S. Pati, P. Banerji, S.B. Majumder, n- to p-type carrier reversal in nanocrystalline indium doped ZnO thin film gas sensors. *Int. J. Hydrog. Energy* **39**, 15134–15141 (2014). <https://doi.org/10.1016/j.ijhydene.2014.07.075>
50. P.M. Ratheesh Kumar, C. Sudha Kartha, K.P. Vijayakumar, T. Abe, Y. Kashiwaba, F. Singh, D.K. Avasthi, On the properties of indium doped ZnO thin films. *Semicond. Sci. Technol.* **20**, 120–126 (2005). <https://doi.org/10.1088/0268-1242/20/2/003>
51. S. Ben Yahia, L. Znaidi, A. Kanaev, J.P. Petitet, Raman study of oriented ZnO thin films deposited by sol–gel method. *Spectrochim. Acta A* **71**, 1234–1238 (2008). <https://doi.org/10.1016/j.saa.2008.03.032>
52. M. Ahmad, J. Zhao, J. Iqbal, W. Miao, L. Xie, R. Mo, J. Zhu, Conductivity enhancement by slight indium doping in ZnO nanowires for optoelectronic applications. *J. Phys. D* **42**, 165406 (2009). <https://doi.org/10.1088/0022-3727/42/16/165406>
53. G.F. Fine, L.M. Cavanagh, A. Afonja, R. Binions, Metal oxide semi-conductor gas sensors in environmental monitoring. *Sensors* **10**, 5469–5502 (2010). <https://doi.org/10.3390/s100605469>
54. R. Biswal, A. Maldonado, J. Vega-Perez, D.R. Acosta, M. De La Luz Olvera, Indium doped zinc oxide thin films deposited by ultrasonic chemical spray technique, starting from zinc acetylacetonate and indium chloride. *Materials* **7**, 5038–5046 (2014). <https://doi.org/10.3390/ma7075038>
55. G. Neri, First fifty years of chemoresistive gas sensors. *Chemosensors* **3**, 1–20 (2015). <https://doi.org/10.3390/chemosensors3010001>
56. T. Yang, W. Jin, Y. Liu, H. Li, S. Yang, W. Chen, Surface reactions of CH₃OH, NH₃ and CO on ZnO nanorod arrays film: DFT investigation for gas sensing selectivity mechanism. *Appl. Surf. Sci.* **457**, 975–980 (2018). <https://doi.org/10.1016/j.apsusc.2018.07.011>
57. S. Pati, P. Banerji, S.B. Majumder, Properties of indium doped nanocrystalline ZnO thin films and their enhanced gas sensing performance. *RSC Adv.* **5**, 61230 (2015). <https://doi.org/10.1039/c5ra10919a>
58. J.H. Lim, S.M. Lee, H.-S. Kim, H.Y. Kim, J. Park, S.-B. Jung, G.C. Park, J. Kim, J. Joo, Synergistic effect of Indium and Gallium co-doping on growth behavior and physical properties of hydrothermally grown ZnO nanorods. *Sci. Rep.* **7**, 41992 (2017). <https://doi.org/10.1038/srep41992>
59. S. Pati, S.B. Majumder, P. Banerji, Role of oxygen vacancy in optical and gas sensing characteristics of ZnO thin films. *J. Alloys Compd.* **541**, 376–379 (2012). <https://doi.org/10.1016/j.jallcom.2012.07.014>
60. H. Jin, H. Zhou, Y. Zhang, Insight into the mechanism of CO oxidation on WO₃ (001) surfaces for gas sensing: a DFT study. *Sensors* **17**, 1898 (2017). <https://doi.org/10.3390/s17081898>
61. C. Wang, L. Yin, L. Zhang, D. Xiang, R. Gao, Metal oxide gas sensors: sensitivity and influencing factors. *Sensors* **10**, 2088–2106 (2010). <https://doi.org/10.3390/s100302088>
62. P. Karnati, S. Akbar, P.A. Morris, Conduction mechanisms in one dimensional core–shell nanostructures for gas sensing: a review. *Sens. Actuators B* **295**, 127–143 (2019). <https://doi.org/10.1016/j.snb.2019.05.049>
63. M. Al-Hashem, S. Akbar, P. Morris, Role of oxygen vacancies in nanostructured metal–oxide gas sensors: a review. *Sens. Actuators B* **301**, 126845 (2019). <https://doi.org/10.1016/j.snb.2019.126845>
64. C.S. Prajapati, D. Visser, S. Anand, N. Bhat, Honeycomb type ZnO nanostructures for sensitive and selective CO detection. *Sens. Actuators B* **252**, 764–772 (2017). <https://doi.org/10.1016/j.snb.2017.06.070>
65. N.H. Ha, D.D. Thinh, N.T. Huong, N.H. Phuong, P.D. Thach, H.S. Hong, Fast response of carbon monoxide gas sensors using a highly porous network of ZnO nanoparticles decorated on 3D reduced graphene oxide. *Appl. Surf. Sci.* **434**,

- 1048–1054 (2018). <https://doi.org/10.1016/j.apsusc.2017.11.047>
66. A. Singh, A. Sharma, M. Tomar, V. Gupta, Growth of highly porous ZnO nanostructures for carbon monoxide gas sensing. *Surf. Coat. Technol.* **343**, 49–56 (2018). <https://doi.org/10.1016/j.surfcoat.2017.11.020>
67. H. Gong, J.Q. Hu, J.H. Wang, C.H. Ong, F.R. Zhu, Nanocrystalline Cu-doped thin film gas sensor for CO. *Sens. Actuators B* **115**, 247–251 (2006). <https://doi.org/10.1016/j.snb.2005.09.008>

Publisher's Note Springer Nature remains neutral with regard to jurisdictional claims in published maps and institutional affiliations.